Is there a sub-parsec-scale jet base in the nearby dwarf galaxy NGC 4395?

(article starts on next page)

Is there a sub-parsec-scale jet base in the nearby dwarf galaxy NGC 4395?

Jun Yang [1]★ Xiaolong Yang [2]★ Joan M. Wrobel,[3] Zsolt Paragi [4] Leonid I. Gurvits [4,5] Luis C. Ho,[6,7] Kristina Nyland,[8] Lulu Fan [9,10] and Daniel Tafoya[1]

[1]*Department of Space, Earth and Environment, Chalmers University of Technology, Onsala Space Observatory, SE-439 92 Onsala, Sweden*
[2]*Shanghai Astronomical Observatory, Key Laboratory of Radio Astronomy, Chinese Academy of Sciences, 200030 Shanghai, China*
[3]*National Radio Astronomy Observatory, P.O. Box O, Socorro, NM 87801, USA*
[4]*Joint Institute for VLBI ERIC (JIVE), Oude Hoogeveensedijk 4, NL-7991 PD Dwingeloo, the Netherlands*
[5]*Faculty of Aerospace Engineering, Delft University of Technology, Kluyverweg 1, NL-2629 HS Delft, the Netherlands*
[6]*Kavli Institute for Astronomy and Astrophysics, Peking University, 100871 Beijing, China*
[7]*Department of Astronomy, School of Physics, Peking University, 100871 Beijing, China*
[8]*U.S. Naval Research Laboratory, 4555 Overlook Ave SW, Washington, DC 20375, USA*
[9]*CAS Key Laboratory for Research in Galaxies and Cosmology, Department of Astronomy, University of Science and Technology of China, 230026 Hefei, China*
[10]*School of Astronomy and Space Sciences, University of Science and Technology of China, Anhui, 230026 Hefei, China*

ABSTRACT

NGC 4395 is a dwarf galaxy at a distance of about 4.3 Mpc (scale: $\sim$0.021 pc mas^{-1}). It hosts an intermediate-mass black hole (IMBH) with a mass between $\sim$10^4 and $\sim$10^5 solar masses. The early radio observations of NGC 4395 with the very long baseline interferometry (VLBI) network, High Sensitivity Array (HSA), at 1.4 GHz in 2005 showed that its nucleus has a sub-mJy outflow-like feature (E) extending over 15 mas. To probe the possibility of the feature E as a continuous jet with a base physically coupled with the accretion disc, we performed deep VLBI observations with the European VLBI Network (EVN) at 5 GHz, and analysed the archival data obtained with the HSA at 1.4 GHz in 2008, NSF's Karl G. Jansky Very Large Array (VLA) at 12–18 GHz and the Atacama Large Millimetre/submillimetre Array (ALMA) at 237 GHz. The feature E displays more diffuse structure in the HSA image of 2008 and has no compact substructure detected in the EVN image. Together with the optically thin steep spectrum and the extremely large angular offset (about 220 mas) from the accurate optical *Gaia* position, we explain the feature E as nuclear shocks likely formed by the IMBH's episodic ejection or wide-angle outflow. The VLA and ALMA observations find a sub-mJy pc-scale diffuse feature, possibly tracing a thermal free–free emission region near the IMBH. There is no detection of a jet base at the IMBH position in the VLBI maps. The non-detections give an extremely low luminosity of $\leq$4.7 $\times$ 10^{33} erg s^{-1} at 5 GHz and indicate no evidence of a disc-jet coupling on sub-pc scales.

Key words: galaxies: active – galaxies: dwarf – galaxies: individual: NGC 4395 – radio continuum: galaxies.

1 INTRODUCTION

Low-mass galaxies including dwarf galaxies (stellar mass $M_\star \leq 10^{9.5}$ M$_\odot$) are expected to host black holes (BHs) with masses close to their 'birth' values (e.g. Greene, Strader & Ho 2020; Volonteri, Habouzit & Colpi 2021) because they underwent less merging and intensive accretion events than their larger counterparts. These low-mass BHs with masses 10^2 M$_\odot$ $\leq M_{bh} \leq 10^6$ M$_\odot$ are usually classified as intermediate-mass black holes (IMBHs). Hunting for IMBHs in low-mass galaxies can help to probe the co-evolution of galaxies and massive BHs (e.g. Greene & Ho 2006, 2007; Kormendy & Ho 2013; Baldassare et al. 2020; Reines 2022).

When IMBHs accrete, they can reveal themselves as low-mass active galactic nuclei (AGNs). Currently, there are several hundred IMBH candidates (fraction <1 per cent of low-mass galaxies)

found by optical and X-ray observations of low-mass galaxies (e.g. Greene & Ho 2007; Reines, Greene & Geha 2013; Pardo et al. 2016). However, only a few of these IMBH candidates (Greene et al. 2020) have sufficiently robust mass constraints for them to be considered as bonafide IMBHs (e.g. Greene & Ho 2006; Baldassare et al. 2015; Woo et al. 2019).

NGC 4395 hosts one of the lowest mass accreting IMBHs known. NGC 4395 is a nearby well-resolved dwarf galaxy at redshift $z = 0.001\,06$ and hosts an extremely low-luminosity Seyfert 1 nucleus (Filippenko & Sargent 1989; Filippenko, Ho & Sargent 1993; Ho, Filippenko & Sargent 1995). Filippenko & Ho (2003) first pointed out that the AGNs might be energized by an IMBH with a mass between $\sim$10^4 and $\sim$10^5 M$_\odot$. Estimates of the IMBH mass are presented in several follow-up studies (e.g. Peterson et al. 2005; Edri et al. 2012; den Brok et al. 2015; La Franca et al. 2015; Brum et al. 2019; Woo et al. 2019). However these mass estimates still have relatively large uncertainties. The early optical reverberation observations found that the central IMBH in NGC 4395 has a mass

★ E-mail: jun.yang@chalmers.se (JY); yangxl@shao.ac.cn (XY)

of $M_{bh} = (3.6 \pm 1.1) \times 10^5$ M$_\odot$ (Peterson et al. 2005). Recently, Woo et al. (2019) have performed another reverberation-based mass measurement and reported a smaller mass, $M_{bh} = 10^{4.0 \pm 0.4}$ M$_\odot$ (including systematic errors).

Jets are frequently found in supermassive and stellar-mass BH accretion systems (cf. a review by Blandford, Meier & Readhead 2019). The innermost parts of continuous radio jets are referred to as jet bases, sometimes also called radio cores. They are partially optically thick and have relatively flat spectra at frequencies $\lesssim 10$ GHz. Detections of jet bases provide direct support for a physical coupling between the jets and their BH accretion discs (e.g. Merloni, Heinz & di Matteo 2003; Fender, Belloni & Gallo 2004; Fischer et al. 2021).

IMBHs are also expected to launch continuous radio jets. About 0.3 per cent of dwarf galaxies from the sample of Reines et al. (2020) have radio counterparts in the Faint Images of the Radio Sky at Twenty Centimetres (FIRST; Becker, White & Helfand 1995) survey. High-resolution observations, including using the very long baseline interferometry (VLBI) technique, have been performed to search for jets that provide independent evidence of IMBH accretion and ejection activity in a sample of dwarf galaxies with wandering IMBH candidates (Sargent et al. 2022) and some nearby low-mass galaxies, e.g. GH 10 (Greene & Ho 2006; Greene, Ho & Ulvestad 2006; Wrobel et al. 2008), POX 52 (Thornton et al. 2008), ESO 243 − 49 HLX-1 (Webb et al. 2012; Cseh et al. 2015), Henize 2–10 (Reines & Deller 2012; Schutte & Reines 2022), Mrk 709 (Reines et al. 2014), and NGC 404 (Paragi et al. 2014; Nyland et al. 2017; Davis et al. 2020). VLBI detections of compact radio cores would provide data points for filling the mass gap between supermassive and stellar-mass BHs (e.g. Greene et al. 2020) and probing some mass-dependent scaling relations (e.g. the Fundamental Plane relation, Merloni et al. 2003; Saikia et al. 2018; Fischer et al. 2021). To date, pc-scale compact radio components have been reported in a few dwarf galaxies: the candidate satellite galaxy of NGC 5252 (Yang et al. 2017; Mezcua et al. 2018; Kim et al. 2020), SDSS J090613.77 + 561015.2 (Yang et al. 2020b) and NGC 4395 (Wrobel, Fassnacht & Ho 2001; Wrobel & Ho 2006). However, there is no evidence of a continuous pc-scale jet with a flat-spectrum radio core in dwarf AGNs. These observational data on the IMBH jets play a key role as starting points for future studies of the IMBH population at radio wavelengths with the next-generation arrays (e.g. Greene et al. 2020; Liodakis 2022).

NGC 4395 has been observed by various radio arrays: the historical Very Large Array (VLA) at multiple frequencies (e.g. Sramek 1992; Becker et al. 1995; Moran et al. 1999; Ho & Ulvestad 2001), NSF's Karl G. Jansky VLA with very wide bandwidths (≥ 2 GHz, King et al. 2013; Saikia et al. 2018; Lacy et al. 2020), the enhanced Multi-Element Remotely Linked Interferometre Network (e-MERLIN) at 1.5 GHz (Baldi et al. 2021), the Very Long Baseline Array (VLBA) at 1.4 GHz (Wrobel et al. 2001) and the High Sensitivity Array (HSA) at 1.4 GHz (Wrobel & Ho 2006). Since the host galaxy has some diffuse radio emission, the observed total flux density shows significant dependence on the image resolution. At 1.4 GHz, its radio nucleus shows a compact structure with a flux density of 1.17 ± 0.15 mJy in the FIRST image (Becker et al. 1995). In the high-resolution 1.4-GHz HSA image, it displays an outflow-like feature extending over 15 mas with a total flux density of 0.74 ± 0.05 mJy (Wrobel & Ho 2006). That HSA image from 2005 is also shown in Fig. 1. The simultaneous radio and X-ray monitoring observations of NGC 4395 (King et al. 2013) displayed a hint for a pc-scale disc–jet coupling in the low-mass AGNs and implied the existence of a jet base. To investigate whether the elongated feature includes a jet base powered
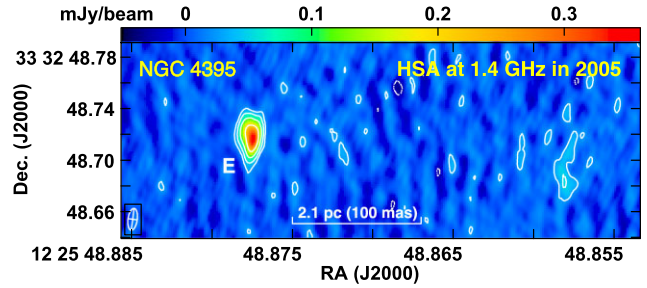

Figure 1. The sub-pc-scale outflow-like feature of NGC 4395 observed previously by Wrobel & Ho (2006) with the HSA at 1.4 GHz on 2005 May 1. The contours start from 0.025 mJy beam^{-1} (2.5σ) and increase by factors $-2, -1, 1, 2, 4$, and 8. The peak brightness is 0.357 mJy beam^{-1}. The full width at half maximum (FWHM) of the synthesized beam is 17.0×7.2 mas at position angle $-8\overset{\circ}{.}0$.

by the central accreting IMBH, we conducted VLBI observations with the EVN at 5.0 GHz and re-analysed the existing archival data observed with the HSA at 1.4 GHz in 2008, the Jansky VLA at 12–18 GHz in 2016 and the Atacama Large Millimetre/submillimetre Array (ALMA) at 237.1 GHz in 2018–2019.

This paper is organized as follows. We introduce the radio observations and the data reduction in Section 2, present multifrequency imaging results of NGC 4395 in Section 3, and discuss radio and optical astrometry precisions, describe the interpretation of the multiscale radio morphology and present potential implications in Section 4. We give our conclusions in Section 5. Throughout the paper, a standard ΛCDM cosmological model with $H_0 = 71$ km s^{-1} Mpc^{-1}, $\Omega_m = 0.27$, $\Omega_\Lambda = 0.73$ is adopted. For our target, this gives a luminosity distance of 4.5 Mpc, fully in agreement with the Cepheid distance 4.3 ± 0.3 Mpc presented by Thim et al. (2004). We define the spectral index α with the power-law spectrum $S(\nu) \propto \nu^\alpha$.

2 OBSERVATIONS AND DATA REDUCTION

In this section, the related radio observations and the methods of our data reduction are reported. We give the details on the high-resolution VLBI observations and the data reduction in Sections 2.1 and 2.2, summarize the VLBI experiment setups in Table 1 and list some basic information on the VLBI calibrators in Table 2. Furthermore, we describe the high-frequency VLA and ALMA observations and data calibration in Sections 2.3 and 2.4, and list the setup and the calibrator information of the multi-epoch ALMA observations in Table 3.

2.1 The EVN experiment at 5 GHz

We observed NGC 4395 with all the available EVN and e-MERLIN telescopes at 5.0 GHz for 6 h during the e-EVN session 2022 January 18–19. There were 17 participating telescopes: Jodrell Bank Lovell (JB1) and Mk2 (JB2), Westerbork (WB, single dish), Effelsberg (EF), Medicina (MC), Tianma (T6), Onsala (ON), Toruń (TR), Yebes (YS), Svetloe (SV), Zelenchukskaya (ZC), Badary (BD), Hartebeesthoek (HH), Cambridge (CM) Knockin (KN), Pickmere (PI), and Defford (DE). All the EVN stations used dual circular polarization and 2-bit quantization. The observations were performed with a maximum date rate of 2048 Mbps (16 32-MHz sub-bands). Due to the limited network bandwidths, the Russian stations (SV, Zc, and BD) had 8 32-MHz sub-bands and the e-MERLIN stations (JB1, CM, KN,

Table 1. Summary of the EVN and HSA observations of NGC 4395.

Project code	Starting time (duration) (UTC)	Freq. (GHz)	Rate (Mbps)	Participating VLBI stations (see Section 2 for the definition of the station codes)
EY039	2022 Jan 18, 23.0 h (6 h)	4.99	2048	JB1, JB2, WB, EF, MC, T6, ON, TR, YS, SV, ZC, BD, HH, CM, KN, PI, DE
BW089	2008 May 04, 23.5 h (8 h)	1.41	512	BR, EF, FD, GB, HN, KP, LA, MK, OV, PT, SC, Y27, AR

Table 2. Summary of the VLBI phase-referencing calibrators. The positional error σ_{pos} is estimated with respect to the ICRF3 (Charlot et al. 2020).

Project code	Array	Calibrator	RA (J2000)	Dec. (J2000)	σ_{pos} (mas)	S_{int} (mJy)	Separation (°)	Structure
EY039	EVN	J1220 + 3343	$12^h20^m33\overset{s}{.}87550$	$+33°43'12\overset{''}{.}0278$	0.2	125 ± 6	1.1	One-sided core-jet source
EY039	EVN	J122755.50 + 334526.9	$12^h27^m55\overset{s}{.}48611$	$+33°45'26\overset{''}{.}9515$	0.2	20 ± 1	0.5	Slightly elongated jet
BW089	HSA	J1220 + 3431	$12^h20^m08\overset{s}{.}29416$	$+34°31'21\overset{''}{.}7427$	0.8	190 ± 9	1.5	One-sided core-jet source

Table 3. Summary of the ALMA experiments of NGC 4395 in 2018–2019 and the calibrator information.

Date	Configuration	Min-Max baseline (m)	Amplitude/Bandpass[a] J1229 + 0203	Phase[b] J1221 + 2813	TOS[c] (min)	Number of antennas
2018 Mar 22	extended configuration	15–784	4.8 Jy; α = -0.83	373 ± 3 mJy	18	46
2018 Aug 28	extended configuration	15–782	6.0 Jy; α = -0.75	433 ± 5 mJy	18	44
2019 Jan 23	compact configuration	15–314	3.6 Jy; α = -0.91	253 ± 2 mJy	7	48

[a]Assumed flux and spectral index α at 230.3 GHz.
[b]Derived flux at 230.3 GHz.
[c]Time on the science source NGC 4395.

PI, and DE) gave 2 64-MHz sub-bands. The data correlation was done in real time by the EVN software correlator SFXC (Keimpema et al. 2015) at JIVE (Joint Institute for VLBI ERIC) using the typical correlation parameters for continuum experiments: 0.5-MHz frequency resolution and 1-s integration time.

The VLBI observations were conducted in the phase-referencing mode (e.g. Rioja & Dodson 2020). We used J1220 + 3343 as the main phase-referencing calibrator. This source is one of those that define the third realization of the International Celestial Reference Frame (ICRF3; Charlot et al. 2020). Its position is listed in Table 2. The calibrator is separated by 1°.1 from the target, has a flat radio spectrum and shows a core-jet structure with a correlated amplitude of $\geq$40 mJy on the long baselines in the geodetic VLBI observations at 2.3 and 8.4 GHz (Charlot et al. 2020). We observed the pair of sources with a cycle time of 8 min (50 s for the calibrator, 390 s for the target, 40 s for two slewing gaps). To improve the phase-referencing calibration further, we also observed a faint source VLASS J122755.50 + 334526.9 (Gordon et al. 2021) as a nearby calibrator for one 2.5-min scan per half hour. The faint calibrator is separated by 29 arcmin from NGC 4395, and has a rising spectrum with total flux densities of ∼17 mJy in the Karl G. Jansky Very Large Array Sky Survey (VLASS) at 2–4 GHz (Lacy et al. 2020; Gordon et al. 2021) and ∼12 mJy in the historical VLA survey FIRST (Becker et al. 1995).

The National Radio Astronomy Observatory (NRAO) Astronomical Image Processing System (AIPS version 31DEC21, Greisen 2003) software package was used to calibrate the visibility data. We followed the general EVN data calibration strategy. First, the no-fringe data were flagged out. Second, a priori amplitude calibrations were performed. Third, the ionospheric dispersive delays were removed. Fourth, the phase errors due to the antenna parallactic angle variations were corrected. Fifth, the instrumental phase and delay offsets across sub-bands were solved via manual fringe fitting on the 2-min data of the source OQ 208. Sixth, the fringe-fitting on

the calibrator data was performed with a solution interval of ∼1 min. To get high-precision solutions, we subtracted the structural phase errors of the main phase-referencing calibrator and combined the data from all the sub-bands. To gain accurate phase interpolations between scans, we smoothed the fringe rate solution using a median filter with a width of half hour. Seventh, the instrumental bandpass shapes were corrected. Eighth, both the amplitude and phase self-calibrations were performed for J1334 + 3044. The output solutions were applied to both VLASS J122755.50 + 334526.9 and NGC 4395. Finally, a phase self-calibration was performed on the data of the faint calibrator VLASS J122755.50 + 334526.9 and its solutions were transferred to NGC 4395. All the related AIPS tasks were called via the PARSELTONGUE interface (Kettenis et al. 2006) and integrated in a single script.

The deconvolution was performed in DIFMAP (Shepherd, Pearson & Taylor 1994). The calibrator J1334 + 3044 shows a core-jet structure with a total flux density of 125 ± 6 mJy at 5.0 GHz. The VLASS J122755.50 + 334526.9 shows a slightly resolved jet structure with a total flux density of 20 ± 1 mJy at 5.0 GHz.

2.2 The HSA data at 1.4 GHz

The imaging results of NGC 4395 from the HSA observations at 1.4 GHz on 2005 May 1 were published by Wrobel & Ho (2006). There were also follow-up HSA observations at 1.4 GHz carried out on 2008 May 4. To get independent imaging results, we reduced the latter HSA data. The observations had a recording data rate of 512 Mbps (8 MHz filters, 2 bit quantization, 16 sub-bands in dual polarization). NGC 4395 was observed for ∼8 h in the phase-referencing mode with a cycle time of ∼5 min. The participating stations were St. Croix (SC), Hancock (HN), Fort Davis (FD), Los Alamos (LA), Pie Town (PT), Kitt Peak (KP), Owens Valley (OV), Brewster (BR), Mauna Kea (MK), Green Bank (GB), phased-up VLA (Y27), Arecibo (AR), and EF.

Table 4. List of the existing high-accuracy radio and optical coordinates of the AGN in NGC 4395.

Method	RA (J2000)	σ_{RA} (mas)	Dec. (J2000)	$\sigma_{Dec.}$ (mas)	Reference
HSA	$12^h25^m48^s.8774$	6	$+33°32'48''.715$	6	Wrobel & Ho (2006)
Gaia DR3	$12^h25^m48^s.85994$	1.4	$+33°32'48''.7110$	1.4	Gaia Collaboration et al. (2022)
Pan-STARRS1	$12^h25^m48^s.86002$	13.4	$+33°32'48''.7063$	4.9	Chambers et al. (2016)

The experiment was designed with the same phase-referencing strategy as described by Wrobel & Ho (2006). The correlation was done by the VLBA correlator in two passes. We reduced the data following the VLBA continuum data calibration method recommended by the AIPS cookbook[1] in Appendix A. Both the HSA and EVN calibration strategy are consistent with each other. For unknown reasons, the station Y27 had very noisy amplitude calibration data. To avoid potential undesirable effect on calibration, these input calibration data were not used and the amplitude calibration of Y27 were achieved by the amplitude self-calibration. The normalization of the amplitude solutions was done without Y27. The off-source visibility data (about 1 min) at the scan beginning of Y27 and AR were also flagged out. We noticed that there were significant residual phase errors ($\sim$100°) on the baselines to AR in the dirty map. Because of this issue, the data of AR were excluded in the final imaging results. The HSA observations used a different calibrator (J1220 + 3431) from that in the EVN observations, while its position is also consistent with the one in ICRF3 (cf. Table 2). The faint target NGC 4395 was imaged without self-calibration.

2.3 The Jansky VLA data at 12–18 GHz

NGC 4395 was also observed by Saikia et al. (2018) with the Jansky VLA (project code 16B–189) in A configuration at 12–18 GHz on 2016 December 15. During the broad-band observations, NGC 4395 was observed for 4 min. The calibrator 3C 286 was observed as the primary flux density calibrator (Perley & Butler 2017). The phase-referencing calibrator was J1215 + 3448 and had a position error of 10 mas with respect to the ICRF3. In the image published by Saikia et al. (2018), it displays a faint two-component structure. To study the two components in detail, we revisited the data. The data reduction was performed using the Common Astronomy Software Applications package (CASA; McMullin et al. 2007). With the VLA pipeline,[2] the data were calibrated and processed.

2.4 The ALMA data at 237 GHz

We retrieved data from the ALMA science archive (project code: 2017.1.00572.S). NGC 4395 was observed in Band 6 on three epochs: 2018 March 22 and August 28, and 2019 January 23. The observations were taken with the ALMA 12-m array in two configurations providing nominal angular resolutions of 0''.8 (extended configuration) and 1''.9 (compact configuration). Quasars J1221 + 2813 and J1229 + 0203 were used for phase-referencing and amplitude/bandpass calibration purposes, respectively. The details of the observational setup are given in Table 3. The data corresponding to each of the configurations were calibrated separately by the ALMA pipeline using CASA versions 5.1.1–5 (extended configuration) and 5.4.0–68 (compact configuration). The calibrated data from both

configurations were concatenated. For each of the configurations, as well as for the combined data, line-free channels were used to create continuum images. The resulting total aggregate bandwidth is 6.9 GHz, centred around 237.1 GHz. The rms noise level of the final continuum images ranges from 0.03 to 0.05 mJy beam^{-1}.

3 MULTIFREQUENCY IMAGING RESULTS

Table 4 lists the accurate positions of NGC 4395 reported by the previous HSA phase-referencing observations at 1.4 GHz (Wrobel & Ho 2006), the optical *Gaia* astrometry (Gaia Collaboration 2021, 2022), and the Panoramic Survey Telescope and Rapid Response System (Pan-STARRS1; Chambers et al. 2016). The systematic positional error (1.4 mas), i.e. the excess noise reported by the *Gaia* data release 3 (DR3) due to various factors (source structure et al.), is included in the error budget. The Pan-STARRS1 position uncertainty contains a systematic uncertainty that came from a comparison of the *Gaia* and Pan-STARRS1 catalogues (Chambers et al. 2016).

Fig. 2 displays the total intensity images of NGC 4395 observed with the VLA at 12–18 GHz, the HSA at 1.4 GHz and the EVN at 5 GHz. These images have a scale of 0.021 pc mas^{-1} and an origin at the position observed by Wrobel & Ho (2006) with the HSA. The radio nucleus has been resolved into two relatively discrete features, labelled as E and C, in the VLA image. The component E can be divided into a very extended sub-component E1 and a faint compact sub-component E2 in the high-resolution HSA image. Fig. 3 shows the ALMA detection of NGC 4395 at 237 GHz. To characterize these components, we also fit the data to point-source and Gaussian models. During the fitting process, we started to fit each relatively discrete image feature to a simple point-source model. If the point-source model gave some $\lesssim 5\sigma$ noise peaks in the residual map, we would fit the feature to the more complex circular or elliptical Gaussian model. In case of the broad-band VLA observations, we also included the spectral index in the models. The fitting results including the formal uncertainties are summarized in Table 5. The formal uncertainties are estimated via normalizing the reduced χ^2 to unity. The flux densities for each component are also plotted in Fig. 4.

With the VLA observations at 12–18 GHz, Saikia et al. (2018) revealed an elongated structure in the radio nucleus of NGC 4395. Our independent data reduction and imaging analysis have fully confirmed those imaging results. The component C is located at the *Gaia* position, shows a diffuse structure with a size of 143 ± 17 mas (3.0 ± 0.3 pc) and has an in-band spectral index $\alpha = +0.6 \pm 0.7$. The component E has an in-band spectral index of $\alpha = -1.6 \pm 0.5$. The estimates of the in-band spectral indices have a large uncertainty because of the very limited observing bandwidth and the faintness of the two components. Only the component E is clearly detected in the HSA image.

The wide-field VLBI images are displayed in the right-hand panels of Fig. 2. The *Gaia* position (Gaia Collaboration 2021) is marked as a white plus and has a separation of 218 mas (4.6 pc) with respect to the HSA position (Wrobel & Ho 2006). The HSA image of 2008

---

[1] http://www.aips.nrao.edu/cook.html
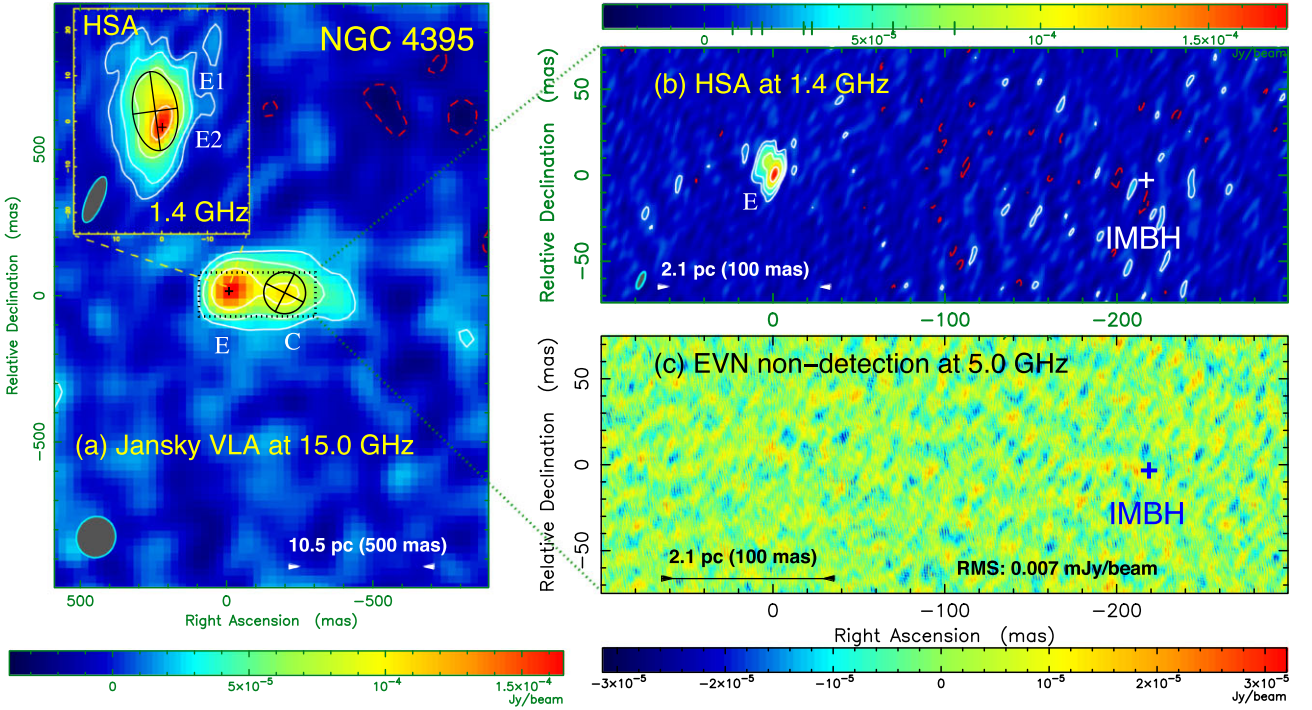[2] https://science.nrao.edu/facilities/vla/data-processing/pipeline

Figure 2. Total intensity images of the nearby low-mass AGN NGC 4395. North is up and east is left. All the images were made with natural weighting. In each image, the origin (0, 0) represents the position from the HSA observations of 2005 (cf. Table 4). The contours give the levels $2.5\sigma \times (-1, 1, 2, 4,...)$. The ellipse in the bottom-left corner plots the shape of the beam FWHM. In the VLBI images, the white and blue pluses mark the optical *Gaia* position (cf. Table 4). (a) The 15-GHz total intensity image made via fitting the VLA visibility data (Saikia et al. 2018) to a point-source model (E) plus a circular Gaussian model (C). The first contours are 0.023 mJy beam^{-1} (2.5σ). The peak brightness is 0.165 mJy beam^{-1}. The FWHM of the synthesized beam is 141×133 mas. The inset shows the HSA intensity image made via fitting the visibility data to an elliptical Gaussian model (E1) and a point source model (E2). In the images, these models are also plotted as the black pluses, the ellipse and the circle to show their positions and sizes (cf. Table 5). (b) The HSA 1.4-GHz CLEAN image. The fist contours are 0.017 mJy beam^{-1} (2.5σ). The peak brightness is 0.173 mJy beam^{-1}. The beam FWHM is 10.8×3.6 mas at position angle $-22°.8$. (c) The EVN 5.0-GHz dirty image. The image has a sensitivity of 0.007 mJy beam^{-1} and a resolution of 3.13×0.95 mas.
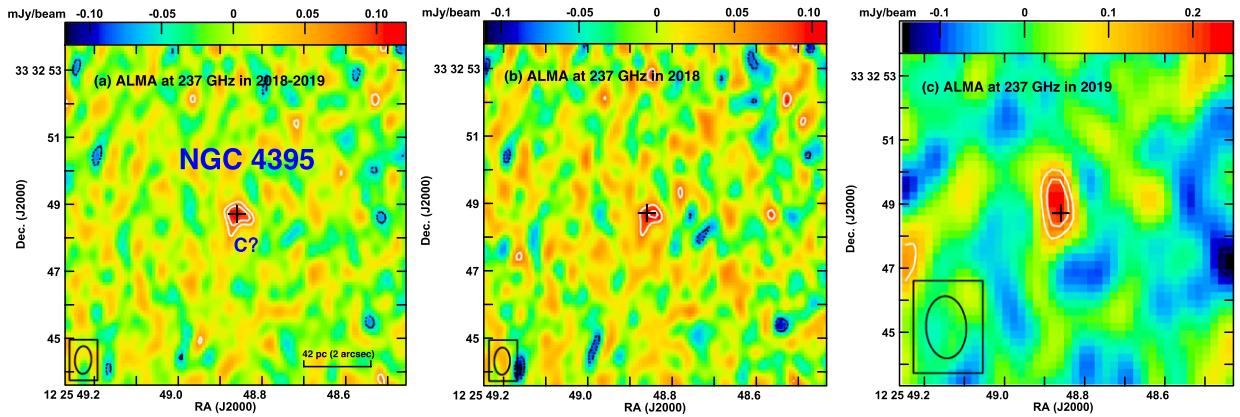
Figure 3. The continuum images of the NGC 4395 nucleus observed by the ALMA at 237.1 GHz. The black plus gives the optical *Gaia* position. (a) The intensity map made by us via combining all the visibility data from 2018–2019 and using a robust parameter of 0.5 in CASA. The contours start from 0.061 mJy beam^{-1} (2.5σ) and increase by factors -1, 1, and 1.4. The peak brightness is 0.112 mJy beam^{-1}. The beam FWHM is 0.83×0.49 arcsec at position angle $-2°.5$. (b) The archival continuum map from the high-resolution observations on 2018 March 22 and August 28. The contours start from 0.071 mJy beam^{-1} (2.5σ) and increase by factors -1.4, -1, 1, and 1.4. The peak brightness is 0.107 mJy beam^{-1}. The beam FWHM is 0.81×0.47 arcsec at position angle $-2°.1$. (c) The archival continuum map from the low-resolution observations on 2019 January 23. The contours start from 0.128 mJy beam^{-1} (2.5σ) and increase by factors -1, 1, and 1.4. The peak brightness is 0.231 mJy beam^{-1}. The beam FWHM is 1.94×1.25 arcsec at position angle $+2°.9$.

in Fig. 2 has an image quality significantly better the HSA image of 2005 (Wrobel & Ho 2006). Owing to the long baselines to EF, the beam area synthesized with natural weighting has become 2.6 times smaller. Because of the two-times higher observing bandwidth, the

image sensitivity has been improved by a factor of 1.4. The outflow-like feature E is clearly detected with a signal-to-noise ratio (SNR) of about 25. The component E is significantly resolved with a size of 17.5 ± 0.9 mas (0.35 ± 0.02 pc). Due to the very high image

Table 5. Summary of the model fitting results of the HSA and VLA visibility data in DIFMAP. For the relative RA and Dec., we take the early HSA position (Wrobel & Ho 2006) as the reference point. In the last column, we use the letters EG for the elliptical Gaussian model, PS for the points source model, and CG for the circular Gaussian model.

Label	Array	Freq. (GHz)	Delta RA (mas)	Delta Dec. (mas)	S_{int} (mJy)	θ_{maj} (mas)	θ_{min} (mas)	θ_{pa} (°)	α	Model type
E1	HSA	1.41	$+1.34 \pm 0.21$	$+2.47 \pm 0.53$	0.652 ± 0.035	17.5 ± 0.9	9.9 ± 1.7	7.7 ± 3.7		EG
E2	HSA	1.41	-0.23 ± 0.25	-1.05 ± 0.47	0.069 ± 0.009					PS
E	HSA	1.41	$+0.87 \pm 0.14$	$+1.35 \pm 0.36$	0.699 ± 0.033	15.8 ± 0.7	8.9 ± 1.3	7.7 ± 3.2		EG
E	VLA	15.00	-8.52 ± 3.60	15.59 ± 3.60	0.158 ± 0.011				-1.6 ± 0.5	PS
C	VLA	15.00	-198.76 ± 9.20	9.87 ± 9.20	0.213 ± 0.022	143.0 ± 17.0	143.0 ± 17.0		$+0.6 \pm 0.7$	CG
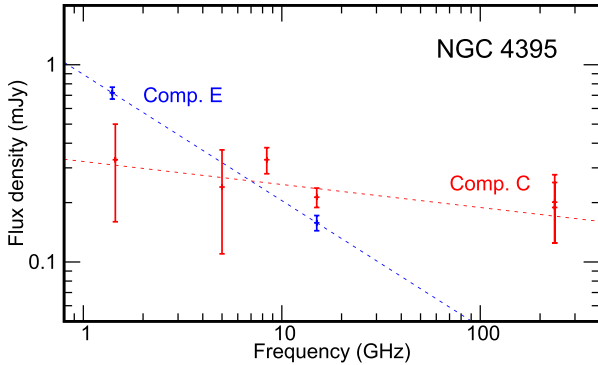
Figure 4. The non-simultaneous radio spectra of the components E and C in the radio nucleus of NGC 4395. The error bars are at the level 1σ and include a 5 per cent systematic error. The spectral indices and the 1σ uncertainties are $\alpha = -0.64 \pm 0.05$ for the component E (2 blue data points) and $\alpha = -0.12 \pm 0.08$ for the component C (6 red data points). The data points of the component C at 1.4–8.4 GHz are estimated based on the total flux densities of the radio nucleus reported in literature and the radio spectrum of the component E (cf. section 4.2 for more details).

resolution, its peak brightness has decreased to 0.173 mJy beam^{-1} and it is hard to directly see the diffuse emission around the peak feature in the CLEAN map. However, this is easily seen in the residual map after the peak feature is subtracted. With an elliptical Gaussian model (E1) and a point source model (E2), we recover a total flux density of 0.72 ± 0.05 mJy, where the error is the quadratic sum of a 5 per cent systematic error and the formal error. The two models are also displayed in the inset of Fig. 2a. The sub-component E1 is a very faint feature and only contributes 10 per cent of total flux density of the component E. Adding the faint sub-component E1 allows us to accurately reveal the peak feature of the component E. Compared to the CLEAN image, this image is made with the model fitting and recovers slightly more diffuse emission on the short baselines and plainly displays the large-scale diffuse emission. To determine the centroid of the entire structure E, we also fit the visibility data to a single elliptical Gaussian model. This is not a very accurate fitting because it gives some significant noise peaks in the residual map and a slightly low total flux density. All these results are consistent with the HSA imaging results reported previously by Wrobel & Ho (2006) and further confirms that it is a non-thermal component with an average brightness temperature of $T_b = (2.3 \pm 0.4) \times 10^6$ K at 1.4 GHz. Wrobel & Ho (2006) also briefly mentioned a 5σ candidate feature near (<50 mas) the *Gaia* position, while its existence cannot be confirmed in the 1.4 times more sensitive image.

The component E is not detected at a level of SNR >5 in the 5-GHz EVN image. This is because of the steep spectrum and the absence of a compact feature. Assuming no significant time variability, we can derive a spectral index of $\alpha = -0.64 \pm 0.05$ for

the component E in Fig. 4. This is in agreement with the early report $\alpha = -0.60 \pm 0.08$ observed by Ho & Ulvestad (2001) between 1.4 and 5 GHz with their arcsec-resolution images. We have also searched the region covering the *Gaia* position but did not detect the component C. The two new VLBI images have reached a quite high sensitivity, ~0.007 mJy beam^{-1}. This gives us a 5σ upper limit of 0.035 mJy beam^{-1} ($T_b = 5.9 \times 10^5$ K) for the peak brightness at 5 GHz of any compact feature.

In the ALMA archival continuum images at 237 GHz, Fig. 3, NGC 4395 is detected at SNR = 3.8 on 2018 March 22 and SNR = 4.5 on 2019 January 23. Its total flux densities are 0.20 ± 0.08 and 0.19 ± 0.06 mJy. To localize the feature precisely, we also combined their visibility data and made a new image, shown in Fig. 3a. The black plus denotes the optical *Gaia* position. Within the 1σ error ellipse ($\sigma_{RA} = 0.062$ mas, $\sigma_{Dec.} = 0.086$ mas), its position is consistent with the *Gaia* position. The average flux density is 0.18 ± 0.06 mJy. It is a slightly resolved feature with a size of $(0.89 \pm 0.21) \times (0.72 \pm 0.14)$ mas. Because of the very limited image quality (SNR = 4.6), the size estimate may not be reliable.

4 DISCUSSION

4.1 Location of the accreting IMBH

The IMBH displaying significant optical variability (e.g. Woo et al. 2019) is inferred to be located at the *Gaia* position (cf. Table 4). The *Gaia* photometry shows that NGC 4395 has a mean magnitude of $m_g = 16.7$. Generally, the multi-epoch full-sky *Gaia* astrometry has reached a position uncertainty of 0.05 mas for compact objects with $m_g = 17.0$ mag in the catalogue of the DR3 (Gaia Collaboration 2021, 2022). The sub-arcsec-resolution optical observations of NGC 4395 show that it has a compact nucleus with a radius <100 mas (e.g. Matthews et al. 1999; Brum et al. 2019). The nucleus is also significantly brighter than any other objects in the *g*-band optical image of Pan-STARRS1 with a field size of 20 × 20 arcsec. Thus, its optical centroid can be unambiguously and accurately located by the long-term *Gaia* astrometry. In Table 4, the independent astrometry from the optical Pan-STARRS1 survey fully supports the *Gaia* astrometry. The positional offset between the two optical positions is very small (5 mas) and within the 1σ error ellipse.

The accreting IMBH cannot be hosted by the component E because of its extremely large angular offset (218 mas) to the *Gaia* position. The HSA and EVN images have a precision of ~1 mas with respect to the optical *Gaia* frame. The two phase-referencing calibrators that are used to locate NGC 4395 in the VLBI observations also have the precise *Gaia* positions available. The separations between the *Gaia* and ICRF3 positions are small, 1.2 mas for J1220 + 3431 and 0.2 mas for J1220 + 3343. Moreover, the *Gaia* astrometry of compact AGNs generally has no significant systematic errors of >10 mas with

respect to the radio cores of VLBI catalogues (e.g. Petrov, Kovalev & Plavin 2019; Yang et al. 2020a; Titov et al. 2022).

4.2 Nature of the components E and C

NGC 4395 is a Seyfert galaxy. In the image from the optical integral field unit (IFU) observations, the ratio [O III]λ5007/Hβ is in the range 5.5–11.0 and has a peak at the optical centroid. This supports the entire nuclear region hosting the components C and E being ionised by the central accreting IMBH instead of by star formation (Brum et al. 2019). Moreover, the total star-forming rate is very low, 0.03 $M_\odot$ yr^{-1} (Smirnova et al. 2020).

The EVN non-detection of the steep-spectrum component E further strengthens the case that it is a very diffuse feature and has no compact jet base. The Jansky VLA monitoring observations at 8.4 GHz show that it has no significant variability on time-scales of days (King et al. 2013). The arcsec-scale compact radio nucleus was first observed by Sramek (1992) and Moran et al. (1999) with the A-configuration VLA at 5.0 GHz on 1982 February 8 and had a flux density of 0.56 ± 0.12 mJy. The second-epoch VLASS survey reported that it had flux densities 0.82 ± 0.24 mJy at 2–4 GHz on 2020 September 12 (Lacy et al. 2020). Assuming a stable radio spectrum with a spectral index of $\alpha = -0.60 \pm 0.08$ (Ho & Ulvestad 2001), the recent VLASS detection supports there being no large flux density variability over about four decades. Due to the relatively stable flux density and the non-circular structure, the component E cannot be naturally identified as a young supernova or a supernova remnant. The possibility of it being a compact starburst has been excluded because of its high brightness temperature ∼10^6 K and no evidence of starbursts in the nuclear region (Brum et al. 2019). Using the high-resolution *Hubble Space Telescope*, Woo et al. (2019) identified a biconical [O III] outflow along the east–west direction in NGC 4395. The position of the component E is consistent with the outer edge of the outflow. Furthermore, there exists some high ionization and high density molecular gas with a size ≲1 arcsec (see figs 5 and 13, Brum et al. 2019) in the eastern region. In view of these observational findings, the non-thermal and steep-spectrum feature E probably represents sub-pc-scale shocks. These shocks may provide additional energy to heat the surrounding gas and strengthen the H_2 and [Fe II] emission lines imaged by Brum et al. (2019) with the optical IFU observations. Shocks are also found in NGC 404 (Nyland et al. 2017). The shocks in NGC 404 have a size up to 20 pc at 12–18 GHz, show an optically thin radio spectrum and likely originate from an outflow.

These shocks in NGC 4395 might result from a continuous outflow from the IMBH or from fading ejecta launched by an episode of IMBH activity. The very low brightness temperature (2.3 ± 0.4) × 10^6 K indicates no significant Doppler beaming effect (e.g. Readhead 1994). The non-detection of the significant offset between the two HSA observations supports that the component E has a very low transverse speed, <0.01 c, where c is the light speed.

The sub-mJy ALMA feature is likely associated with the component C instead of the component E. Its centroid is consistent with the optical *Gaia* position (cf. Section 3). Furthermore, its flux densities are tentatively consistent with the low-frequency spectrum of the component C. Fig. 4 shows the non-simultaneous radio spectra of the components E and C. Using the radio spectrum of the component E and the total flux densities observed by the *e*-MERLIN at 1.4 GHz (Baldi et al. 2021) and the VLA at 5 and 8.4 GHz (Sramek 1992; Moran et al. 1999; King et al. 2013), we also derived the flux densities of the component C at frequencies ≤8.4 GHz. The indirect measurements are also reliable because these

images have sub-arcsec resolutions and the entire radio nucleus is not significantly resolved. The three data points are also plotted in Fig. 4. Because the component E has a steep spectrum with $\alpha = -0.64 \pm 0.05$, the data points at 237 GHz are quite consistent with the extrapolation of the spectra of the component C. There is no evidence for a strong absorption at the lower observing frequencies. The broad-band radio spectrum can be described by a single power law function. The best-fitting model for the non-simultaneous spectrum between 1.4 and 237 GHz is $S_\nu = (0.32 \pm 0.08)\nu^{-0.12 \pm 0.08}$. Because of the large uncertainty (10–50 per cent) of these flux density measurements, the spectral index estimate is only sensitive to large (≳30 per cent) flux density variability. We caution that the estimate also has a certain bias because of different image resolutions and possible non-uniform absorption at very low frequencies. Moreover, the component C might have a more complex radio spectrum. Future VLA and ALMA observations, at matched angular resolutions, could add the more data points between 15.0 and 237.1 GHz and thus test the assumption of the single power law spectrum.

The central pc-scale component C possibly originates from thermal free–free emission instead of non-thermal synchrotron emission. Firstly, its average brightness temperatures are very low: $T_b = 56 \pm 9$ K in the 15 GHz VLA map and ≤5.9×10^5 K in the 1.4-GHz HSA and 5-GHz EVN maps. Secondly, its radio morphology is very extended, 143 ± 17.0 mas at 15 GHz. There is no sub-pc-scale compact component detected in the VLBI maps. Finally, its broad-band radio spectrum tends to be relatively flat ($\alpha = -0.12 \pm 0.08$). A flat radio spectrum can also come from a partially optically thick synchrotron jet base (cf. a recent review by Blandford et al. 2019). However, the jet base will have a quite high brightness temperature of >10^6 K and show a conical structure.

If the diffuse component C is a thermal emission region, it may result from a clumpy torus (e.g. Netzer 2015; Gámez Rosas et al. 2022; Isbell et al. 2022). The diffuse feature has a radius of ∼1.4 pc at 15 GHz and its centroid coincides with the IMBH. As a clumpy torus including a polar outflow, it is slightly larger than that observed in the archetypal type 2 galaxy NGC 1068 (e.g. Gallimore, Baum & O'Dea 2004; Gámez Rosas et al. 2022), while ∼200 times smaller than the first-known thick torus directly imaged in Cygnus A (Carilli et al. 2019). Combes et al. (2019) studied the molecular tori of seven nearby Seyfert galaxies and reported the radii in the range 6–27 pc. Compared to these Seyfert galaxies, NGC 4395 is expected to have a relatively small torus (cf. a review by Netzer 2015) because of its very low M_{bh} (e.g. Woo et al. 2019) and bolometric luminosity (e.g. Brum et al. 2019). The observed radius of ∼1.4 pc is consistent with the expected outer edge of the torus, which is naturally considered as the gravitational sphere of influence of the IMBH ($R_{BH, sph}$). By adopting $M_{bh} = 10^{4-5}$ $M_\odot$ and velocity dispersion $\sigma_\star = 18$ km s^{-1} (Woo et al. 2019), the estimated $R_{BH, sph}$ is ∼1.0 pc according to equation (3) in Netzer (2015). Near infrared IFU observations by Brum et al. (2019) reveal a slightly extended H_2 emission line region in the nucleus of NGC 4395. The molecular H_2 region also roughly covers the thermal radio emission region. Because of the limited image sensitivity and the near face-on disc geometry, there is no evidence of a recognisable disc structure in the radio maps.

4.3 Implications

A sub-mJy mas-scale compact radio core is frequently seen at ≲5 GHz in AGNs (e.g. Deller & Middelberg 2014; Herrera Ruiz et al. 2017; Fischer et al. 2021; Yang et al. 2021). Its existence represents a continuous and partially optically thick jet base associated with

the accreting massive black hole (e.g. Blandford et al. [2019]). If there is a compact jet base formed by the central accreting IMBH of NGC 4395, the HSA and EVN non-detections at the *Gaia* position allow us to set the 5σ upper limits on its luminosity, $L_R = \nu L_\nu = 1.3 \times 10^{33}$ erg s^{-1} at 1.4 GHz and $L_R = 4.7 \times 10^{33}$ erg s^{-1} at 5.0 GHz. For nearby AGNs (e.g. Giroletti & Panessa [2009]; Baldi et al. [2021]; Fischer et al. [2021]), radio non-detections can generally reach a luminosity upper limit of $\sim 10^{35}$ erg s^{-1}. Thus, the two luminosity limits for NGC 4395 are quite stringent. VLBI non-detections of the radio cores are also reported in low-mass AGNs, e.g. Henize 2–10 (Reines & Deller [2012]) and NGC 404 (Paragi et al. [2014]). These VLBI non-detections indicate that the accreting IMBHs have very weak jet activity or stay in a radio quiescent state (e.g. Greene et al. [2006]).

NGC 4395 shows a strong variability in the full X-ray range (e.g. Kammoun et al. [2019]) and has an absorption-corrected, time-averaged 2–10 keV luminosity, $L_X = 8.8 \times 10^{39}$ erg s^{-1} (Moran et al. [2005]). However, King et al. ([2013]) reported that there is no significant correlation between the radio and X-ray light curves observed simultaneously by the VLA and *Swift* for about two months. Our VLBI non-detection of the jet base is fully in agreement with the very weak correlation because the VLA observations trace the pc-scale extended emission instead of the sub-pc-scale compact jet base near the IMBH.

The Fundamental Plane of BH activity is a statistical relation derived from an incomplete sample of hard-state stellar-mass BHs in X-ray binaries (e.g. Fender et al. [2004]) and supermassive BHs in AGNs. It represents a correlation among X-ray luminosity, radio luminosity, and BH mass, and shows a very large scatter ($\lesssim 1$ dex). This plane potentially supports the existence of a common physical mechanism acting across the mass scales (e.g. Merloni et al. [2003]; Falcke, Körding & Markoff [2004]; Saikia et al. [2018]). NGC 4395 has been frequently used as a precious data point to fill the mass gap of the plane. However, the recent multiresolution VLA and VLBA observations of 25 nearby AGNs by Fischer et al. ([2021]) suggest that the radio luminosity supporting the Fundamental Plane mainly result from the radio emission integrated on the VLA instead of VLBA scales. The VLBI non-detection of NGC 4395 at 5 GHz allows us to add an extremely low radio luminosity point to the plots of the Fundamental Plane relation. Because of the relatively large radio luminosity offset (≥ 0.8 dex) from the Fundamental Plane relation of (Merloni et al. [2003]) at 5 GHz, the data point of NGC 4395 in the mass gap tends to support the recent VLBI results reported by (Fischer et al. [2021]). The radio luminosity of VLBI-scale compact AGN cores at 5 GHz may not follow the prediction of the Fundamental Plane relation.

The component C has a radio luminosity of $L_R = (8.6 \pm 1.0) \times 10^{34}$ erg s^{-1} at 15 GHz. NGC 4395 is a very low-luminosity AGN (Moran et al. [1999]). Its bolometric luminosity L_{bol} is between 1.9×10^{40} and 4.9×10^{41} erg s^{-1} (Brum et al. [2019]). If the thermal nature of the pc-scale component C in such a low-luminosity AGN is confirmed by future radio observations, the large population of the low-luminosity AGNs (cf. a review by Ho [2008]) would allow us to to find additional similar objects in deep sky surveys.

5 CONCLUSIONS

To answer whether there is a sub-pc-scale continuous jet tracing the accreting IMBH in NGC 4395, we carried out deep EVN observations at 5.0 GHz, reduced HSA data at 1.4 GHz and Jansky VLA data at 12–18 GHz, and examined ALMA archival continuum images at 237 GHz. We found that the previously known outflow-like feature

E displays additional diffuse structure in the 1.4-GHz HSA image of 2008, shows a steep spectrum between 1.4 and 15.0 GHz, and has no compact substructure detected in the 5.0-GHz EVN image. Together with the very large angular offset (about 220 mas) from the mas-accuracy optical *Gaia* position, we suggest that the eastern non-thermal feature E traces nuclear shocks probably due to prior IMBH ejection activity. In the VLA and ALMA images, we also identified a 100-mas-scale feature C surrounding the accreting IMBH. Because of its relatively flat spectrum and VLBI non-detections at 1.4 and 5 GHz, we tentatively interpreted the central pc-scale feature C as a thermal emission region originating from a clumpy torus. Moreover, the deep VLBI images show no evidence for radio emission from a jet base at the *Gaia* position, taken to mark the location of the accreting IMBH. Assuming no strong radio variability, the VLBI non-detection at 5 GHz indicates a very weak jet base at the IMBH, $\leq 4.7 \times 10^{33}$ erg s^{-1}, and no direct evidence of a sub-pc-scale disc–jet coupling above the luminosity limit.

The upcoming high-resolution IFU spectroscopy[3] with the *James Webb Space Telescope* would significantly advance our understanding on the inner structure of the infrared nucleus of NGC 4395 (Seth et al. [2021]). In the future, the next-generation VLA (ngVLA[4]) observations of NGC 4395 would reach an image sensitivity of 0.1 μJy beam^{-1} (2-h on-source time, 8-GHz bandwidth) and a resolution of ~ 1 mas (maximum baseline length 8860 km with a long-baseline array) at 4–12 GHz, possibly revealing an IMBH jet base.

---

[3] https://www.stsci.edu/jwst/science-execution/program-information.html?id = 2016

[4] https://ngvla.nrao.edu/

DATA AVAILABILITY

The correlation data underlying this article are available in the EVN Data Archive (http://www.jive.nl/select-experiment) and the NRAO Science Data Archive. The calibrated visibility data underlying this article will be shared on reasonable request to the corresponding author.

REFERENCES

Baldassare V. F., Reines A. E., Gallo E., Greene J. E., 2015, ApJ, 809, L14
Baldassare V. F., Dickey C., Geha M., Reines A. E., 2020, ApJ, 898, L3
Baldi R. D. et al., 2021, MNRAS, 500, 4749
Becker R. H., White R. L., Helfand D. J., 1995, ApJ, 450, 559
Blandford R., Meier D., Readhead A., 2019, ARA&A, 57, 467
Brum C. et al., 2019, MNRAS, 486, 691
Carilli C. L., Perley R. A., Dhawan V., Perley D. A., 2019, ApJ, 874, L32
Chambers K. C. et al., 2016, preprint (arXiv:1612.05560)
Charlot P. et al., 2020, A&A, 644, A159
Combes F. et al., 2019, A&A, 623, A79
Cseh D. et al., 2015, MNRAS, 446, 3268
Davis T. A. et al., 2020, MNRAS, 496, 4061
Deller A. T., Middelberg E., 2014, AJ, 147, 14
den Brok M. et al., 2015, ApJ, 809, 101
Edri H., Rafter S. E., Chelouche D., Kaspi S., Behar E., 2012, ApJ, 756, 73
Falcke H., Körding E., Markoff S., 2004, A&A, 414, 895
Fender R. P., Belloni T. M., Gallo E., 2004, MNRAS, 355, 1105
Filippenko A. V., Ho L. C., 2003, ApJ, 588, L13
Filippenko A. V., Sargent W. L. W., 1989, ApJ, 342, L11
Filippenko A. V., Ho L. C., Sargent W. L. W., 1993, ApJ, 410, L75
Fischer T. C. et al., 2021, ApJ, 906, 88
Gaia Collaboration, 2021, A&A, 649, A1
Gaia Collaboration, 2022, preprint (arXiv:2206.05681)
Gallimore J. F., Baum S. A., O'Dea C. P., 2004, ApJ, 613, 794
Gámez Rosas V. et al., 2022, Nature, 602, 403
Giroletti M., Panessa F., 2009, ApJ, 706, L260
Gordon Y. A. et al., 2021, ApJS, 255, 30
Greene J. E., Ho L. C., 2006, ApJ, 641, 117
Greene J. E., Ho L. C., 2007, ApJ, 670, 92
Greene J. E., Ho L. C., Ulvestad J. S., 2006, ApJ, 636, 56
Greene J. E., Strader J., Ho L. C., 2020, ARA&A, 58, 257
Greisen E. W., 2003, in Heck A., ed., Astrophysics and Space Science Library, Vol. 285, Information Handling in Astronomy – Historical Vistas. Kluwer, Dordrecht, p. 109
Herrera Ruiz N. et al., 2017, A&A, 607, A132

Ho L. C., 2008, ARA&A, 46, 475
Ho L. C., Ulvestad J. S., 2001, ApJS, 133, 77
Ho L. C., Filippenko A. V., Sargent W. L., 1995, ApJS, 98, 477
Isbell J. W. et al., 2022, preprint (arXiv:2205.01575)
Kammoun E. S. et al., 2019, ApJ, 886, 145
Keimpema A. et al., 2015, Exp. Astron., 39, 259
Kettenis M., van Langevelde H. J., Reynolds C., Cotton B., 2006, in Gabriel C., Arviset C., Ponz D., Enrique S., eds, ASP Conf. Ser. Vol. 351, Astronomical Data Analysis Software and Systems XV. Astron. Soc. Pac., San Francisco, p. 497
Kim M., López K. M., Jonker P. G., Ho L. C., Im M., 2020, MNRAS, 493, L76
King A. L., Miller J. M., Reynolds M. T., Gültekin K., Gallo E., Maitra D., 2013, ApJ, 774, L25
Kormendy J., Ho L. C., 2013, ARA&A, 51, 511
La Franca F. et al., 2015, MNRAS, 449, 1526
Lacy M. et al., 2020, PASP, 132, 035001
Liodakis I., 2022, MNRAS, 512, 291
Matthews L. D. et al., 1999, AJ, 118, 208
McMullin J. P., Waters B., Schiebel D., Young W., Golap K., 2007, in Shaw R. A., Hill F., Bell D. J., eds, ASP Conf. Ser. Vol. 376, Astronomical Data Analysis Software and Systems XVI. Astron. Soc. Pac., San Francisco, p. 127
Merloni A., Heinz S., di Matteo T., 2003, MNRAS, 345, 1057
Mezcua M., Kim M., Ho L. C., Lonsdale C. J., 2018, MNRAS, 480, L74
Moran E. C., Filippenko A. V., Ho L. C., Shields J. C., Belloni T., Comastri A., Snowden S. L., Sramek R. A., 1999, PASP, 111, 801
Moran E. C., Eracleous M., Leighly K. M., Chartas G., Filippenko A. V., Ho L. C., Blanco P. R., 2005, AJ, 129, 2108
Netzer H., 2015, ARA&A, 53, 365
Nyland K. et al., 2017, ApJ, 845, 50
Paragi Z., Frey S., Kaaret P., Cseh D., Overzier R., Kharb P., 2014, ApJ, 791, 2
Pardo K. et al., 2016, ApJ, 831, 203
Perley R. A., Butler B. J., 2017, ApJS, 230, 7
Peterson B. M. et al., 2005, ApJ, 632, 799
Petrov L., Kovalev Y. Y., Plavin A. V., 2019, MNRAS, 482, 3023
Readhead A. C. S., 1994, ApJ, 426, 51
Reines A. E., 2022, Nat. Astron., 6, 26
Reines A. E., Deller A. T., 2012, ApJ, 750, L24
Reines A. E., Greene J. E., Geha M., 2013, ApJ, 775, 116
Reines A. E., Plotkin R. M., Russell T. D., Mezcua M., Condon J. J., Sivakoff G. R., Johnson K. E., 2014, ApJ, 787, L30
Reines A. E., Condon J. J., Darling J., Greene J. E., 2020, ApJ, 888, 36
Rioja M. J., Dodson R., 2020, A&AR, 28, 6
Saikia P., Körding E., Coppejans D. L., Falcke H., Williams D., Baldi R. D., Mchardy I., Beswick R., 2018, A&A, 616, A152
Sargent A. J., Johnson M. C., Reines A. E., Secrest N. J., van der Horst A. J., Cigan P. J., Darling J., Greene J. E., 2022, preprint (arXiv:2205.16006)
Schutte Z., Reines A. E., 2022, Nature, 601, 329
Seth A. C. et al., 2021, Revealing Low Luminosity Active Galactic Nuclei (ReveaLLAGN), JWST Proposal. Cycle 1, ID. #2016
Shepherd M. C., Pearson T. J., Taylor G. B., 1994, Bull. Am. Astron. Soc., 26, 987
Smirnova K. I., Wiebe D. S., Moiseev A. V., Jozsa G. I. G., 2020, Astrophys. Bull., 75, 234
Sramek R., 1992, in Filippenko A. V., ed., ASP Conf. Ser. Vol. 31, Relationships Between Active Galactic Nuclei and Starburst Galaxies. Astron. Soc. Pac., San Francisco, p. 273
Thim F., Hoessel J. G., Saha A., Claver J., Dolphin A., Tammann G. A., 2004, AJ, 127, 2322
Thornton C. E., Barth A. J., Ho L. C., Rutledge R. E., Greene J. E., 2008, ApJ, 686, 892
Titov O. et al., 2022, MNRAS, 512, 874
Volonteri M., Habouzit M., Colpi M., 2021, Nat. Rev. Phys., 3, 732
Webb N. et al., 2012, Science, 337, 554
Woo J.-H., Cho H., Gallo E., Hodges-Kluck E., Le H. A. N., Shin J., Son D., Horst J. C., 2019, Nat. Astron., 3, 755

Wrobel J. M., Ho L. C., 2006, ApJ, 646, L95
Wrobel J. M., Fassnacht C. D., Ho L. C., 2001, ApJ, 553, L23
Wrobel J. M., Greene J. E., Ho L. C., Ulvestad J. S., 2008, ApJ, 686, 838
Yang X. et al., 2017, MNRAS, 464, L70
Yang J., Paragi Z., An T., Baan W. A., Mohan P., Liu X., 2020a, MNRAS, 494, 1744

Yang J., Gurvits L. I., Paragi Z., Frey S., Conway J. E., Liu X., Cui L., 2020b, MNRAS, 495, L71
Yang J. et al., 2021, MNRAS, 503, 3886

This paper has been typeset from a TEX/LATEX file prepared by the author.